Numerical Simulation of Sea Ice and Structure Interaction Using Common Node DEM-SPH Model

April 10, 2024

SHEN Zhong-xiang [a,b] ,WANG Wen-qing [a] ,XU Cheng-yue [a] ,LI Hong-bin [a] ,JIANG Yin [a] ,

LIU Ren-wei [2,*]

* School of Naval Architecture and Ocean Engineering, Jiangsu University of Science and Technology, Zhenjiang 212100, China

[b] College of Harbor,Coastal and Offshore Engineering,Hohai University,Nanjing 210098,China

Abstract

In this work, a novel fluid-structure coupling method called the common node discrete element-smoothed particle hydrodynamics (DS-SPH) method is introduced. This framework combines the principles of the common node discrete element method (DEM) and smoothed particle hydrodynamics (SPH) to construct DEM-SPH particles situated on the same node. By doing so, the DEM particles can interact with the SPH particles within their support domain, enabling fluid-structure interaction (FSI). To determine the DEM microscopic parameters required for this method, uniaxial compression and three-point bending tests are conducted on sea ice. To verify the proposed model, we select the interaction between sea ice and structures as a case study. Through simulation, the model's capability of accurately depicting sea ice deformation and fracture has been demonstrated. The results indicate that the inclusion of SPH particles with fluid properties in the DEM model has minimal impact on the main mechanical parameters of sea ice. Addition-ally, it helps prevent the occurrence of particle splashing during cement failure. However, it is observed that the size of DEM particles and the friction between DEM particles and the structure significantly influence the macroscopic mechanical behavior of the common-node DEM-SPH model. Finally, we compare the fracture behavior of sea ice and the ice forces acting on structures obtained from the current model with on-site measured results. The agreement between the two sets of data is excellent, further validating the effectiveness of the proposed model in practical

appli-cations.

1 1 Introduction

The physical properties of sea ice are the important factors affecting ice loading on the offshore structures operating in ice infested waters. The numerical methods are essential due to the high cost and lengthy duration of model tests. Although data regarding ice loads is valuable, there are lim-itations to its completeness. Typically, the range of parameters is quite narrow, and in some cases, obtaining precise data on ice properties like thickness, strength, and friction can be challenging. Consequently, analyzing the impact of parame-ters on ice loads using full-scale data becomes arduous. However, numerical simulations provide an alternative type of data for investigating ice-structure interaction. Through statistical studies based on simulations, all parameters used are clearly defined and can be adjusted as needed. Addition-ally, it is relatively convenient to conduct simulations withslight variations in parameters, allowing us to examine the sensitivity of the process to these changes. Furthermore, considering the inter-action between sea ice and fluid is imperative for a comprehensive assessment (Ji and Tian, 2021; Liu et al., 2021).

Sea ice is a natural composite material with complex properties (Moslet, 2007; Timco and Weeks, 2010). Its mechanical properties are affected by its internal structure and external loading environment, showing strong discrete characteristics (Liu et al., 2018; Xue et al., 2019, 2020). The effects of temper-ature, brine volume and stress rate on the uniaxial compressive strength of sea ice are analyzed, and the results showed that the uniaxial compressive strength of sea ice increases exponentially with the decrease of temper-ature, showing a negative exponential relationship with the square root of the brine volume, and a linear relationship

—

—

with the loading speed (Wang et al., 2014). The single-factor effect of sea ice brine volume, temperature and loading rate on the sea ice bending strength is analyzed and it is found that the sea ice bending strength has a negative exponential relationship with the square root of the brine volume and a lin-ear relationship with the loading rate, and a double-factor function of sea ice bending strength, brine volume and loading rate is obtained (Ji et al., 2011).

For continuum materials with fracture characteristics, such as rocks and sea ice, the discrete element method (DEM) has demonstrated powerful computational and ana-lytical capabilities. The influence of mesoscopic parameters on macroscopic parameters in the parallel bonding model is studied by combining theoretical analysis and numerical simulation (Yang et al., 2020). The uniaxial tensile and compressive tests of sea ice are simulated and found that only considering the tensile and shear properties of the cement, ignoring the influence of the normal force on the cemented strength, cannot correctly simulate the tensile and compressive strength ratio of the ice (Di et al., 2018). The microscopic fracture process of fresh water ice is studied and the crack fracture characteristics of ice under confined pressure loading are obtained (Sun et al., 2023). Ni et al. (Ni et al., 2020a, 2020b; Ni and Huang, 2020) used the numerical simulation method of three-point bending of sea ice to study the relationship between the discrete element microscopic parameters and the mechanical properties of the overall model, and gave the discrete element microscopic parameter values suitable for ice materials. Researchers (Ji et al., 2017; Long et al., 2019) improved the shear failure strength of the parallel bond model by using the Moore-Coulomb criterion, and a calculation method for estimating discrete element bond strength and internal friction coefficient from sea ice thickness, uniaxial compressive strength and bending strength is established by simulating the uniaxial compression test and three-point bending test of sea ice. A smooth extended polyhedron-based DEM (Dilated Polyhedron-based DEM, DPDEM) based on the Minkowski sum method is constructed by superimposing spherical elements and polyhedron elements. The parameters involved in the bond failure criterion were determined (Liu et al., 2020).

In the study of the fluid-solid coupling problem of gran-ular materials, computational fluid dynamics (CFD) is applied to solve the fluid flow, and is coupled with the ice block simulated by the discrete element method to simulate the ship-ice-fluid interaction (Ji et al., 2017). A floating ice model is established by coupling the discrete element method in the viscous flow CFD solver, and combined with the Euler multiphase flow VOF model to simulate the interaction between the ship and the floating ice (He et al., 2022). The results were in good agreement with the experiment. The repulsive force model is utilized to establish a calculation model for the coupling force between the extended polyhe-dron discrete element and fluid particles. Additionally,researchers developed a fluid-solid coupling method based on the extended polyhedron discrete element method and smooth particle hydrodynamics (Liu et al., 2020; Luo et al., 2020; Tang et al., 2022; Xie et al., 2022). Up until now, the LS DYNA software's capacity to accurately simulate the interaction between sea ice and structures has been under-valued. This work in the current manuscript aims to present a novel discrete element modeling approach and to employ it in simulating the interaction between sea ice and struc-tures. Besides, the DS-SPH model can help prevent the occurrence of particle splashing during cement failure.

This paper presents a novel approach for coupling a common-node discrete element (DEM) method with a smooth particle hydrodynamic (SPH) method to model the fluid-structure interaction. Specifically, it focuses on inves-tigating

the appropriate DEM microscopic parameters for accurately representing the mechanical behavior of sea ice in the coupled DEM-SPH model. The LS-DYNA software is employed to establish DEM and DEM-SPH sea ice models comprising regularly arranged particles. Through numerical simulations of uniaxial compression and three-point bending of sea ice, the study analyzes the impact of discrete element parameters and SPH on the macroscopic mechanical proper-ties of sea ice. Building upon these findings, a mathematical formula is developed for estimating the discrete element parameters based on the macroscopic mechanical properties of sea ice. The formula is further refined to account for the influence of particle radius and friction coefficient on the model's macroscopic mechanical properties. This research provides valuable insights for selecting suitable discrete ele-ment parameters in the common-node DEM-SPH model, and the accuracy of the proposed formula is verified through an illustrative example involving the interaction between sea ice and structures.

2   2 Common-node DEM-SPH method

3   2.1 Basic principle

The DEM and the SPH methods are both numerical approaches used to compute the motion and effects of a large quantity of small particles. In the common-node discrete element-smooth particle hydrodynamic fluid-structure cou-pling method, DEM particles and SPH particles are placed at the same location to form a common-node DEM-SPH particle, as depicted in Fig. 1. This particle, referred to as a DEM-SPH particle or DS particle, enables the interaction of DEM particles with other SPH particles within the support domain of the SPH particle sharing the same node.

The DS model possesses the following characteristics: (1) The mechanical properties of the DS model are primarily governed by DEM particles, with minimal influence from SPH particles. (2) When the structure interacts with the DS model, it exclusively engages with the DEM particles and does not interact with the SPH particles.
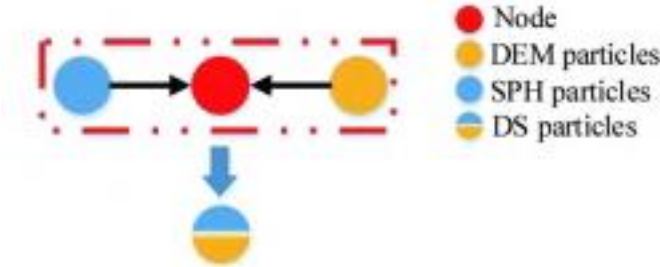

Fig. 1. Schematic diagram of common-node DEM-SPH particles.

4 2.2 Equations of motion

With the assumption,the force F_i of the i -th DS particle is the resultant of force F_{1i} and force F_{2i} calculated by SPH, and the moment M_i is the resultant of moment M_{1i} calculated by the DEM and moment M_{2i} calculated by SPH,which is based on Newton's Second Law:

$$F_i = F_{1i} + F_{2i} = (m_i) \cdot u_i'';$$

$$M_i = M_{1i} + M_{2i} = I_i \theta_i'',$$

where u_i'' is the acceleration of the i -th DS particle, m_i is the total mass of the i -th DS particle,and I_i is the moment of inertia of the i -th DS particle,defined by:

$$m_i = m_{1i} + m_{2i};$$

$$I_i = \frac{2}{5} m_i r_i^2,$$

where m_{1i} is the DEM mass of the i -th DS particle, m_{2i} is the SPH mass of the i -th DS particle,and r_i is the DEM radius of the i -th DS particle.

The direct integration method is employed to solve the equation of motion for the particle. This method calculates the velocity and angular velocity at the current time step based on the acceleration at the same time step, as well as the angular acceleration, velocity and angular velocity from the previous time step. The time step is denoted as Δt ,and it is used to express the interval between each calculation. The velocity and angular velocity are then updated accordingly by:

$$(\theta_i')_{n+1} = (\theta_i')_n + (u_i'')_{n+1} \cdot \Delta t;$$

$$(u_i')_{n+1} = (u_i')_n + (u_i'')_{n+1} \cdot \Delta t.$$

With Eqs. (5) and (6), the displacement and rotation angle can be obtained:

$$(\theta_i)_{n+1} = (\theta_i)_n + (\theta_i')_{n+1} \cdot \Delta t$$

$$(u_i)_{n+1} = (u_i)_n + (u_i')_{n+1} \cdot \Delta t.$$

5 3 Microcosmic parameter of the common node DEM-SPH model

3.1 Microscopic parameter calibration method

The macroscopic mechanical properties of the DEM model are determined by three types of microscopic param-eters: basic particle parameters, particle control parameters, and parallel bonding model parameters. The basic parameters of particles encompass the radius r ,density ρ ,elastic modulus$E$,and Poissons ratio u . Particle contact parameters primarily consist of the normal damping coefficient C_n ,tangential damping coefficient C_s ,internal friction coefficient μ_b ,normal stiffness coefficient N_k ,and tangential stiffness coefficient S_k . The parameters of the parallel bond model mainly include bond normal stiffness p_n ,bond tangential stiffness p_s ,normal bond strength of cementation b_n ,tangential bond strength of cementation b_s ,and bond radius coefficient p_r .

The contact force between particles is determined by a combination of particle basic parameters and particle control parameters. In the case of the parallel bonding model for bonded discs, the force and failure are influenced by particle basic parameters, particle control parameters, and the parameters specific to the parallel bonding model. Within the current DS model, the interaction force between DEM and SPH particles affects the behavior of the particles. As a result, the process of determining the DEM parameters fol-lows these steps: Firstly, a set of particles with regularly arranged particle radii is selected to create uni-axial com-pression DEM and DEM-SPH sea ice models. These models are then subjected to numerical simulations of uniaxial com-pression on sea ice, combined with relevant theories, to ana-lyze the impact of discrete element parameters and SPH on macroscopic properties such as compression elastic modu-lus, Poisson's ratio, and compression strength of sea ice. Next, using the same particle radius and arrangement, a three-point bending DEM and DEM-SPH sea ice model are constructed, and relevant theories are employed to perform numerical simulations of three-point bending. The objective of this analysis is to investigate how discrete element parameters and SPH influence the macroscopic bending elastic modulus and bending strength of sea ice. Finally, a functional relationship between microscopic parameters and macroscopic parameters is established.

6   3.2 Uniaxial compression simulation

The uniaxial compression DEM model is shown in Fig. 2. The model size is 20 cm×20 cm×50 cm$(a{\times}a{\times}I)$. The particle arrangement is hexagonal close packing, the particle diameter $d = 20$ mm ,and the particle material density is 9×10^{-10}t/mm^3 . The number of particles is 3906 . The lower plate is fixed, and the vertical loading speed of the upper plate is 10 mm/s .

When the compressive displacement of the plate is Δl , the axial strain of the discrete element sea ice is $\varepsilon = \Delta l / l$. Assuming that the normal stiffness of the particle is k and the overlapping amount x_i of the i -th particle on the boundary and the pressure plate, the total force between the pressure plate and the sea ice is:

$$F = f_s{\times}k\sum x_i,$$

where f_s is the contact stiffness scaling factor,and k is the particle normal stiffness determined by
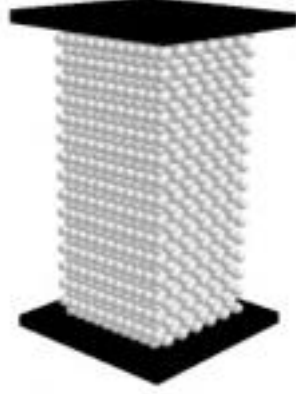

Fig. 2. Uniaxial compression DEM model.

$$k = \frac{Er}{3(1-2u)} \times N_k,$$

where E is the elastic modulus of the granular material, r is the radius of the particle, u is the Poissons ratio of the granular material, N_k is the normal stiffness coefficient of the particle, and the value is 0.01 .

The compressive elastic modulus of sea ice is:

$$E_c = \frac{F}{\varepsilon a^2}.$$

From Eqs. (9), (10) and (11), we can obtain:

$$\frac{E}{1-2u} = \frac{3E_c\varepsilon a^2}{f_s \times N_k r \sum x_i}.$$

According to the parallel bonding model, the bonding normal force and tangential force between particles are:

$$f_\mathrm{n} = p_\mathrm{n} \times \Delta u_\mathrm{n};$$

$$f_\mathrm{s} = p_\mathrm{s} \times \Delta u_\mathrm{s},$$

where Δu_n and Δu_s are particle normal relative displacement and particle tangential relative displacement respectively, p_n . p_s are cementation normal stiffness and cementation tangen-tial stiffness respectively, when the radius of the bonding particle is r ,we obtain:

$$p_\mathrm{n} = \frac{\pi r}{2} \times p_r^2 \times b_\mathrm{c};$$

7

$$p_{\mathrm{s}} = p_{\mathrm{n}} \times z,$$

where r is the particle radius, p_r is the cementation radius coefficient, b_{e} is the cementation modulus, and z is the ratio of cementation tangential to normal stiffness, which is rep-resented by p_s/p_{n} below.

To facilitate a smooth transition from the cohesive force to the contact force upon cement failure, minimize particle splashing and ensure the stability of the calculation system, it is crucial that the contact force between particles be kept smaller, or preferably significantly smaller than the cohesive force during cement failure. Consequently:

$$\frac{E}{1-2u} < \frac{3\pi \times p_r^2 \times b_c}{N_k}.$$

In the uniaxial compression DEM model, it is essential to have similar or closely matched overlapping sizes x_i between the particles and the platen. Assuming the average overlapping size is x, the distance between the particles at both ends is denoted by $y = l - \Delta l + 2x$, and the actual axial deformation is represented by $\Delta l - 2x$. In order to maintain a constant macroscopic elastic modulus of sea ice and keep the force between the pressure plate and sea ice consistent, adjustments are required when the particle normal stiffness k decreases. Specifically, when the particle normal stiffness k decreases, it is necessary to increase the overlapping size x_i between the particles and the pressure plate. Conse-quently, this leads to an increase in the distance y between the particles at both ends, resulting in a decrease in the actual axial deformation Δu. Additionally, the relative dis-placement between the bonded particles decreases. To maintain a balanced interaction force between the interme-diate particles and the system, it is crucial to increase the normal stiffness of the bond or tangential stiffness. Simi-larly, if the particle normal stiffness k increases, it becomes necessary to reduce the normal stiffness or tangential stiffness of the cemented bonds. This adjustment ensures that the dis-crete element sea ice's macroscopic elastic modulus remains unchanged.

Poisson's ratio represents the relationship between the transverse normal strain and the axial normal strain when a material experiences unidirectional tension or compression. The lateral strain of sea ice primarily depends on the actual axial deformation and the ratio of cemented tangential to normal stiffness. In order to achieve a close match between the actual axial deformation and the compressive displace-ment of the pressure plate, and to align the transverse strain to axial strain ratio of the DEM model with the macroscopic Poisson's ratio of sea ice, it is necessary to decrease the overlapping size of the particles and the pressure plate.

Replacing x with $0.05\Delta l$ in Eq. (12), we obtain:

$$\frac{E}{1-2u} \times f_{\mathrm{s}} = \frac{6000 E_{\mathrm{c}} a^2}{rnl},$$

where n is the number of particles in contact between the sea ice DEM and the plate. Taking the particle Poisson's ratio as 0.3 ,when the elastic modulus is 1200MPa ,the value of $E \times f_s$ is 1.829×10^5MPa .

The friction coefficient between discrete element particles and structure is 0.014 , and the values of particle control parameters are shown in Table 1. C_n and C_s are related to the rebound coefficient, mass and stiffness of particle elements (Liu et al.,2020). Considering that C_n, C_s and S_k/N_k have little influence on the damage of discrete element com-pression and bending, to simplify the parameter calibration process, the values remain unchanged.

In Fig. 3, the addition of SPH particles to each particle in the DEM model allows for the creation of a DEM-SPH model subjected to uniaxial compression. While the DEM and SPH models share nodes, they do not directly interact. The internal forces between the SPH particles and external

Table 1 Particle control parameters

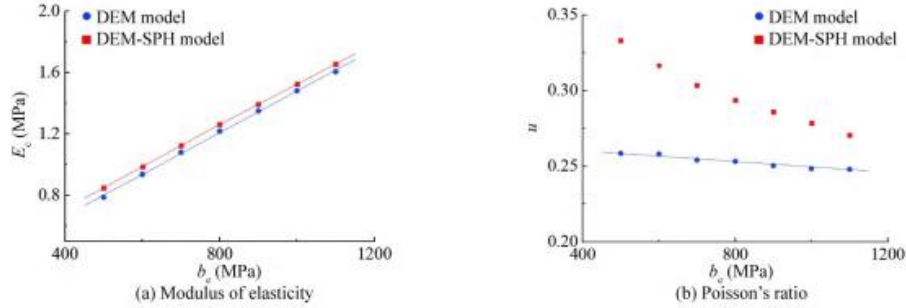|	
Normal damping coefficient C_n	0.7
Tangential damping coefficient C_s	0.4
Internal friction coefficient μ_b	0.3
Normal stiffness coefficient N_k	0.01
Tangential to normal stiffness ratio S_k/N_k	0.29

Fig. 3. Uniaxial compression DEM-SPH model.

forces from other SPH particles are transmitted through these nodes. In comparison with the DEM model, the DEM-SPH model incorporates interaction forces between SPH particles, necessitating careful selection of SPH parameters to minimize their impact on the mechanical properties of sea ice within the DEM-SPH model.

To achieve similarity between the sea ice mechanical properties of the DEM-SPH model and the DEM model, specific SPH parameter choices are crucial. This paper selects fluid property parameters where the material is considered NULL, the state equation is GRUNEISEN, and the sound velocity is 1.65×10^6 mm/s . To ensure consistency in the calculation step and total mass with the DEM model, the DEM particle density is set to 8×10^{-10}t/mm^3 ,while the SPH particle mass is 4.189×10^{-7}t . Considering the volume determined by the mass and density of SPH particles, and the need to avoid significant density

9

differences when cou-pling the DEM-SPH model with SPH fluid, the density of the SPH particles is chosen as $1 \times 10^{-10} \mathrm{t/mm^3}$.

In the parallel bond model, the determination of the nor-mal stiffness and tangential stiffness of the bond relies on the macroscopic elastic modulus and Poisson's ratio. By examining Eqs. (7) and (8), it becomes evident that, when the particle radius remains constant, the normal stiffness and tangential stiff-ness of the bond exhibit a direct proportionality to the bond modulus. In this context, the tensile and shear strengths of the cement are assigned larger values, while the coefficient of the bond radius is set at 1.0 (Huang et al., 2020). Fig. 4 illustrates the relationship between the com-pressive modulus of elasticity, Poisson's ratio, and the bond modulus of both the DEM and DEM-SPH models when the bonded tangential to normal stiffness ratio equals 0.3 .

During the compression process, the DEM-SPH model exhibits a slightly higher compressive elastic modulus com-pared to the DEM model with the same cemented normal stiffness. For instance, when the compressive elastic modulus is 1200MPa ,the DEM model has a cementation modulus of 789MPa ,while the DEM-SPH model has a cementation modulus of 755MPa . Upon introducing SPH particles,the Poisson's ratio of the DEM-SPH model experiences a noticeable increase in comparison with the DEM model. However, as the cementation modulus increases, the influence of SPH particles on the Poisson's ratio gradually dimin-ishes.

Since the transverse deformation of discrete element sea ice correlates positively with the actual axial deformation, and the actual axial deformation decreases as the cementation modulus increases, the overall trend indicates that the Pois-son's ratio decreases with an increase in the cementation modulus.

The DEM and DEM-SPH models maintain a constant cementation modulus of 789MPa and 755MPa ,respec-tively. Simulation results yield curves depicting the macro-scopic compressive elastic modulus, Poisson's ratio, and the ratio of the cemented tangential to normal stiffness. Fig. 5a illustrates that the compressive elastic modulus in both models remains the same and exhibits a linear relationship with the ratio of the cemented tangential to normal stiffness. Furthermore, Fig. 5b shows that the Poisson's ratio of both models decreases as the ratio of tangential to normal stiffness
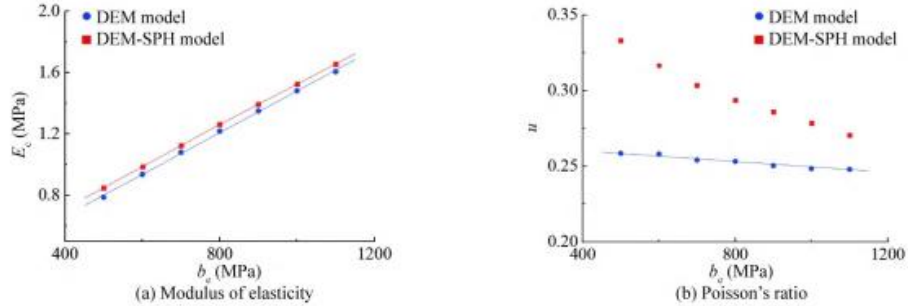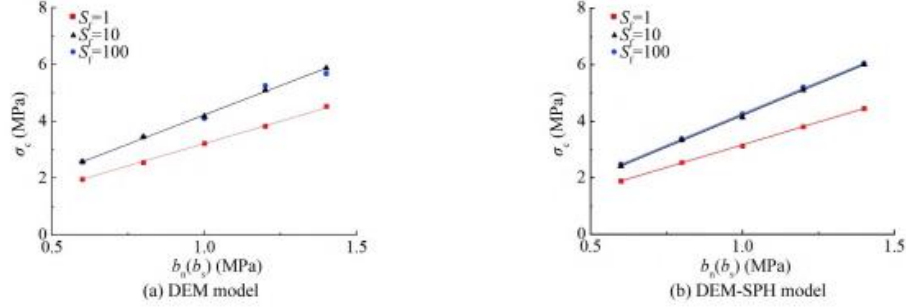

Fig. 4. Influence of cementation modulus.

10

Fig. 5. Influence of tangential to normal stiffness ratio of cementation.

of cementation increases. However, when comparing models with the same cemented tangential to normal stiffness ratio, the DEM-SPH model demonstrates a slightly larger Poisson' s ratio compared with the DEM model.

Based on research conducted on simulating rock fracture (Long et al., 2019), the ratio of cemented normal and tan-gential bond strength is set at 1.0. Through analysis using different f_s values,the relationship between compressive strength and bond strength is illustrated in Fig. 6. Notably, the introduction of SPH particles has minimal impact on compressive strength.

When f_s equals 1,although the contact force between particles is smaller than the cohesive force during cement failure, instability arises due to excessive contact forces between particles, leading to fluctuations in compressive strength. However,as f_s increases to 10 and 100,the com-pressive strength value tends to stabilize, indicating a more consistent behavior.

Considering the calculation stability and the correlation between particle elastic modulus E and compressive elastic modulus E_c, $f_s = 152.38$ and $E = 1200$MPa are chosen. Under a sea ice compressive strength of 4MPa ,the corresponding cemented bond strengths for the DEM model and DEM-SPH model are determined to be 0.96MPa and 0.94MPa , respectively. The stress-strain curves depicting the compres-sive failure of sea ice are presented in Fig. 7.

Fig. 8 demonstrates how the introduction of SPH particlesalters the phenomenon of particle splashing following cement failure. When utilizing fluid parameters and a NULL material equation, the impact on particle splashing primarily pertains to particle mass, density, and the chosen cut-off pressure.

In the absence of SPH particles, the compression failure results are depicted in Fig. 8a. With a small cut-off pressure, the influence of SPH particles on particle splashing is mini-mal, as illustrated in Fig. 8b. However, as the cut-off pressure increases, there is a gradual reduction in particle splashing after cement failure, as evident in Figs. 8c and 8d.

The compressive strength results of the DEM-SPH model under varying internal friction coefficients are pre-sented in Fig. 9. It should be noted that the internal friction coefficient and the normal contact force between particles solely determine the residual tangential force during shear failure of the bond, thus having no effect on the compressive strength (Yang et al., 2006).

11

7   3.3 Three-point bending simulation

Three-point bending models of DEM and DEM-SPH are shown in Fig. 10. The particle arrangement is close-packed hexagonal packing,the model size is 15 cm×15 cm×140 cm ($a×a×b$) ,the particle diameter is 20 mm ,and the density is the same as that in the uniaxial compression model. The total of nodes is 6192 , the span of the support points below the model is 1000 mm ,and the loading velocity is 10 mm/s .
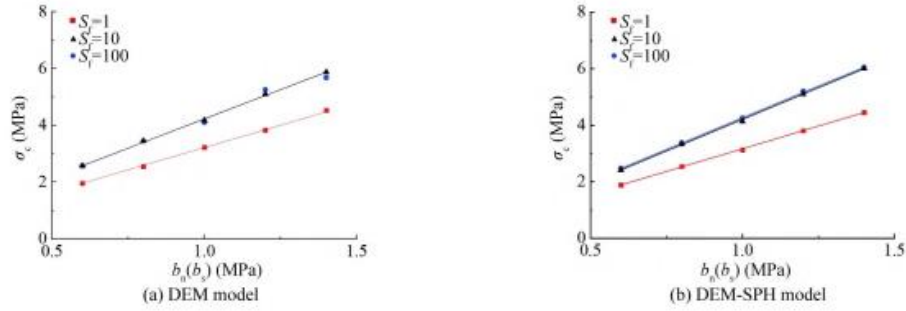

(a) DEM model

(b) DEM-SPH model

Fig. 6. Effect of f_s on compression strength.

(a) Without SPH particles

(b) Cut-off pressure with −100 kPa

(c) Cut-off pressure with −10 kPa
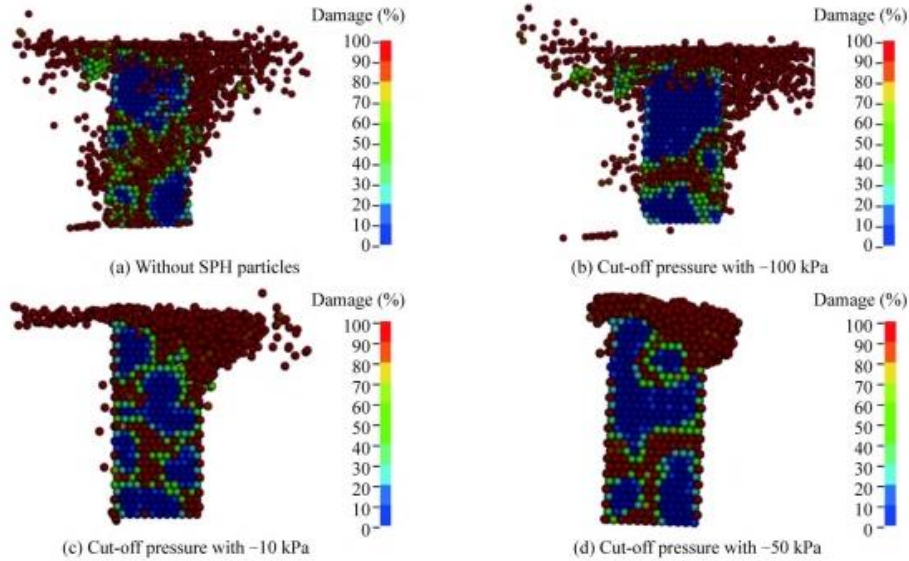
(d) Cut-off pressure with −50 kPa

Fig. 7. Stress-strain curves of uniaxial compression tests.

When the loading displacement is Δa ,the sea ice deflec-tion is Δa . When the normal stiffness of the particle is k and the overlapping size of the i -th

12

particle on the boundary and the upper structure is x_i ,the total force between the pressure plate and the sea ice is $F = f_{\mathrm{s}} \times k \Sigma x_i$,and the macroscopic bending elastic modulus is:

$$E_{\mathrm{b}} = \frac{l^3}{4a^4} \times \frac{F}{\Delta a}.$$

From Eqs. (10) and (19),taking $f_{\mathrm{s}} = 152.38$,we obtain:

$$\frac{E}{1-2u} = \frac{0.07875 E_{\mathrm{b}} a^4 \Delta a}{l^3 N_k r \sum x_i}.$$

The average overlap size between the sea ice and the indenter is x ,then the actual deflection of the sea ice in three-point bending is $\Delta a - 1.5x$. To make the actual deflection close to the loading displacement and reduce the influence of the overlapping size on the calculation results, let $x < 0.05 \Delta a$,then it can be obtained from Eq. (20):

$$\frac{E}{1-2u} \geq \frac{157.5 E_{\mathrm{h}} a^4}{rn^3}.$$

where n is the number of particles in contact between the sea ice DEM and the indenter. When the flexural elastic modulus is 800MPa ,the elastic modulus and Poissons ratio of the granular material obtained by Eq. (21) can be chosen to be the same as the above uniaxial compression simulation. The discrete element parameters of the three-point bending simulation are shown in Table 2.

In Fig. 11a, it is evident that the flexural modulus of the DEM-SPH model slightly exceeds that of the DEM model, considering the influence of particle arrangement and the force between SPH particles during the bending process. Under the same cementation modulus, the cementation modulus values corresponding to a bending elastic modulus of 800MPa are 554MPa and 584MPa ,respectively. Main-taining a constant cementation modulus, Fig. 11b illustrates the relationship between the flexural modulus and the ratio of the cemented tangential to normal stiffness. Both models exhibit a similar bending elastic modulus, which demonstrates a linear association with the ratio of tangential to normal stiffness in cementation.

Fig. 12 presents the curve depicting the relationship between bending strength and bond strength. Considering the influence of SPH particles, the DEM-SPH model exhibits an increased required force for fracture and conse-quently experiences a higher bending strength, even when the bond strength remains constant.

When the bending strength of sea ice is 1.4MPa ,the corresponding bond strengths of DEM model and DEM-SPH model are 0.6MPa and 0.57MPa ,respectively. The
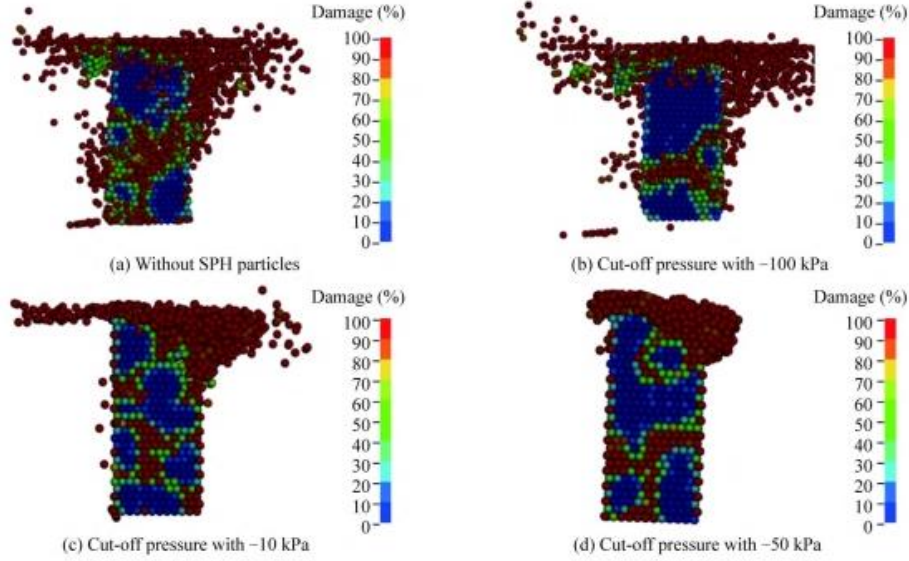
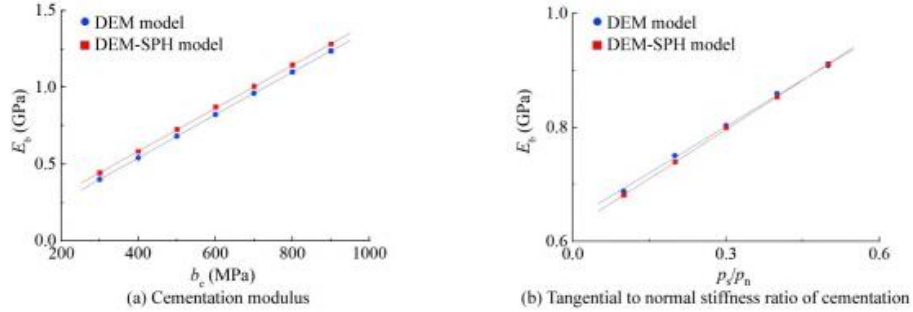Fig. 8. Failure patterns of different SPH parameters.

Fig. 9. Influence of internal friction coefficient on compressive strength.

stress-deflection curve of three-point bending is shown in Fig. 13, and the failure results are shown in Fig. 14.

The cementation will fail in tension as the sea ice bends, so the internal friction coefficient and the tangential bond strength of cementation have no effect on the bending strength. Fig. 15 shows the simulation results of the bendingstrength of the DEM-SPH model under different internal friction coefficients and cemented tangential bond strengths. 4 DEM parameters for common node DEM-SPH model 4.1 Determination of discrete element parameters

From the above work on selected discrete element parameters, it is difficult to simultaneously satisfy compres-sive elasticity modulus, Poisson's ratio, compressive strength, bending elasticity modulus and bending strength. To make

14

the sea ice discrete element parameters model as close as possible to the macro-scopic mechanical properties of sea ice, the selected discrete element parameters should meet the compressive elastic modulus, compressive strength and bending strength.

When sea ice undergoes compression, the cement will fail in tension and shear. While sea ice is in bending defor-mation, the cement will fail in tension. Therefore, we can modify the macro numerical parameters by adjusting the
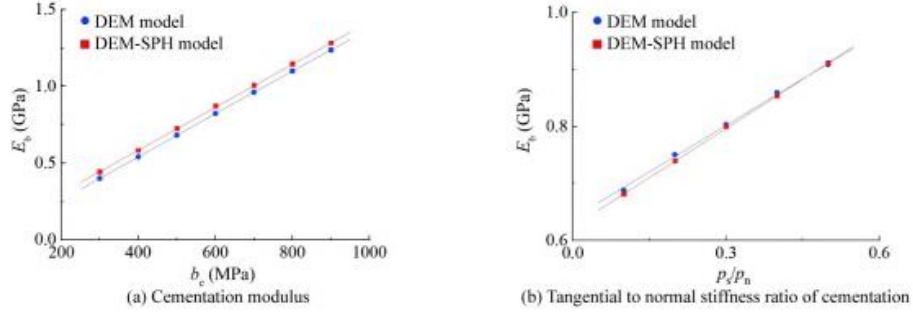

Fig. 10. Three-point bending model.

Table 2 Three-point bending parameters

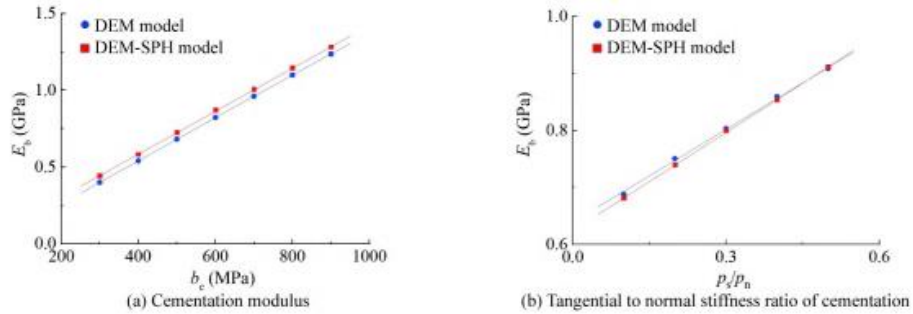| Elastic Modulus E (MPa) | 1200 |
Poissons ratio u	0.3
Normal damping coefficient C_n	0.7
Tangential damping coefficient C_s	0.4
Internal friction coefficient μ_b	0.3
Normal stiffness coefficient N_k	0.01
Ratio of tangential to normal stiffness S_k/N_k	0.29
Ratio of bond tangential to normal stiffness p_s/p_n	0.3
Cementradius coefficient p_r	1.0

Fig. 11. Influence of cementation parameters on bending elastic modulus.

(a) Different coefficient of internal friction   (b) Tangential bond strength of different cementation
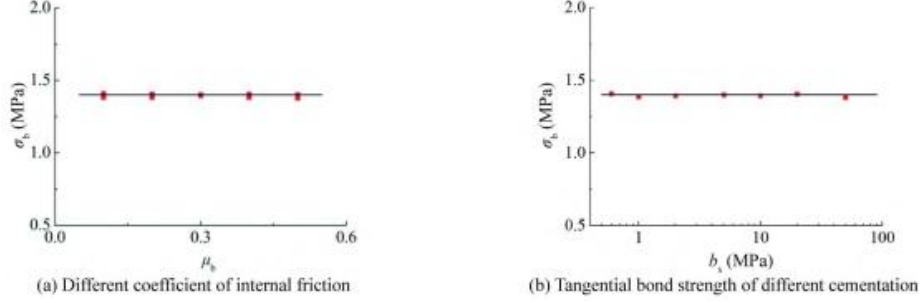
Fig. 14. Failure snapshot of three-point bending test.

(a) Different coefficient of internal friction   (b) Tangential bond strength of different cementation
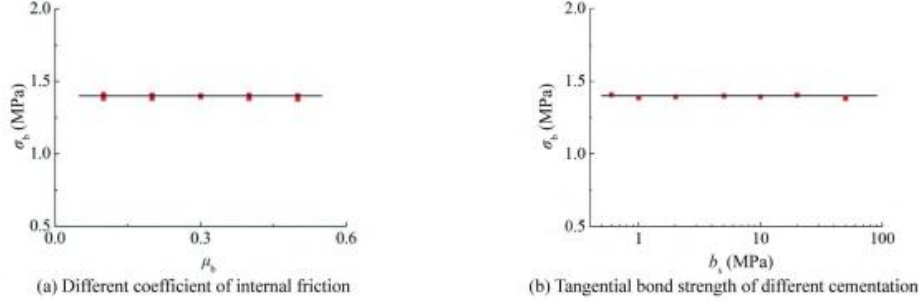
Fig. 15. Bending strength results with different parameters.

normal and tangential stiffness of cementation, the tensile and shear strength of the cement. Thus, the compressive modulus of elasticity is kept constant to obtain multiple groups of cementation modulus and cementation tangential to normal stiffness ratio, then the normal bond strength of cementation can be determined with the bending strength, and then the range of compressive strength can be obtained from setting different tangential bond strengths.

The compressive strength is largely affected by the fric-tion coefficient μ between the discrete element and the structure. When analyzing the discrete element parameters, it is first necessary to select the value of μ ,here $\mu = 0.014$. When the compressive elastic modulus is 1200MPa and the bending strength is 1.4MPa ,the parameters obtained by the above strategy are shown in Table 3. When the ratio of tan-gential to normal stiffness increases, the compressive modu-lus of elasticity and bending strength remain the same unless the normal stiffness of cementation and normal bond

Table 3 Partial cementation parameters obtained from fixing Young's modulus and bending strength

866	0.1
0.752	
807	0.2
0.682	
755	0.3
0.590	
712	0.4
0.541	
664	0.5
0.505	
644	0.6
0.495	

strength of cementation are reduced. The relationship between compressive strength and ratio of tangential to nor-mal bond strength is shown in Fig. 16. When the ratio of tangential to normal stiffness of cementation remains constant, as the ratio of tangential to normal bond strength increases, the compressive strength is limited successively by the tangential bond strength and the normal bond strength, showing a trend of increasing first and then
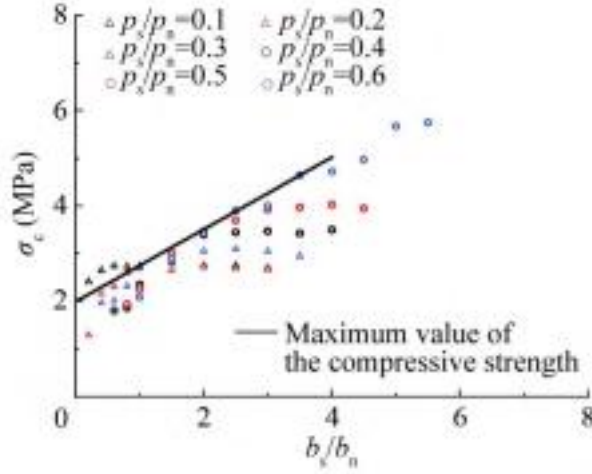

Fig. 16. Relationship between compressive strength and the ratio of tangential to normal bond strength.

remaining unchanged. When the cemented tangential and normal stiffness increases from 0.1 to 0.2 , the peak of the compressive strength decreases with the decrease of the cemented normal bond strength while keeping the bending strength constant; when the cemented tangential to normal stiffness ratio is larger than 0.2 and increases, although the cemented normal bond strength that keeps the bending strength constant decreases, the influence of the cemented tangential bond strength on the compressive strength increases, so the peak of compressive strength increases with the increase of the ratio of tangential and normal stiffness of cementation.

Let z to be the ratio of cemented tangential to normal stiffness,and e to be the ratio of sea ice compression to bending strength. The maximum compressive strength determined from the ratio of tangential to normal bond strength is:

$$\sigma_{\mathrm{c}} = 0.757 b_{\mathrm{s}}/b_{\mathrm{n}} + 2, 0.2 {\leq} z {\leq} 0.6.$$

The reasonable ratio of tangential to normal bond strength corresponding to the maximum compressive strength is:

$$b_{\mathrm{s}}/b_{\mathrm{n}} = 6z {-} 0.3.$$

The functional relationship between z and e is obtained from Eqs. (12) and (13):

$$z = 0.31e {-} 0.39, 0.2 {\leq} z {\leq} 0.6.$$

Finally, the cementation modulus, the normal bond strength and the tangential bond strength are determined as:

$$b_{\mathrm{c}} = E_{\mathrm{c}} \left(0.2991 z^2 {-} 0.5789 z + 0.7764 \right);$$

$$b_{\mathrm{n}} = \sigma_{\mathrm{b}} \left(0.915 z^2 {-} 1.059 z + 0.66 \right);$$

$$b_{\mathrm{s}} = (6z {-} 0.3) b_{\mathrm{n}}.$$

4.2 Correction considering the effect of particle size

For uniaxial compression and three-point bending mod-els, the number of particles in each layer is inversely pro-portional to r^2 . When $\Delta l {-} 2x$ and $\Delta a {-} 1.5x$ are constant,the interparticle normal is proportional to the tangential relative displacement and particle radius r ,the normal relative dis-placement and tangential relative displacement between par-ticles are proportional to the particle radius r ,the normal force and tangential force of the bond between par-ticles are proportional to r^2 ,and the moment on the bonded disc is proportional to r^3 . Therefore,when the particle radius r changes while the cementation mod-ulus and tangential to normal stiffness ratio of cementation are kept unchanged, the total force transmitted between particles remains almost unchanged; when the particle radius r changes while the tensile and shear strength of cementation are kept fixed, the compressive and bending strengths of the model are almost unchanged.

From the Eq. (12),taking $u = 0.3$ and $f_{\mathrm{s}} = 152.38$,we have:

$$E = \frac{15.75 E_{\mathrm{c}} a^2}{rnl},$$

where a^2 is proportional to n, r^2 is inversely proportional to n ,then:

$$E = \frac{50 E_{\mathrm{c}} r}{l}.$$

For uniaxial compression simulation,when $f_{\rm s} = 152.38$ and the value of E is smaller than Eq. (29),the average overlap between discrete elements and finite elements is larger than $0.05\varepsilon l$,and the compression elastic modulus obtained from the simulation decreases; when $f_{\rm s} = 152.38$ and the value of E is larger than that in Eq. (29),the average overlapping amount is smaller than 0.05εl ,and the compres-sive elastic modulus obtained by simulation increases. Con-sidering the generality of the simulation,the value of E is simplified as:

$$E = E_{\rm c}.$$

The values of Eqs. (29) and (30) and the selection of discrete element param-eters are verified in this section. Assuming that the compressive elastic modulus is 800MPa , the compressive strength is 2.4MPa ,and the bending strength is 1MPa ,the main discrete element parameters are selected according to the above work, and other parameters can be found in Table 2.

Utilize the dimensionless size ratio L/D ,where L is the size of the loading section of the sea ice specimen $(L = a), D$ is the diameter of the particle, and the curve of compressive elastic modulus, compressive strength, bending strength and L/D is shown in Fig. 17. It can be found that when the particle diameter is small,i.e., L/D is large,the particle diameter and the particle elastic modulus have little effect on the sea ice elastic modulus or its strength; when the particle diameter becomes larger,i.e., L/D becomes smaller,the elastic modulus and strength of the sea ice decrease due to the decrease of the effective contact area of the model; when the L/D is smaller,the particle elastic modulus E has a great influence on the compressive elastic modulus of sea ice. For this case, the effect is more obvious with a smaller number of parti-
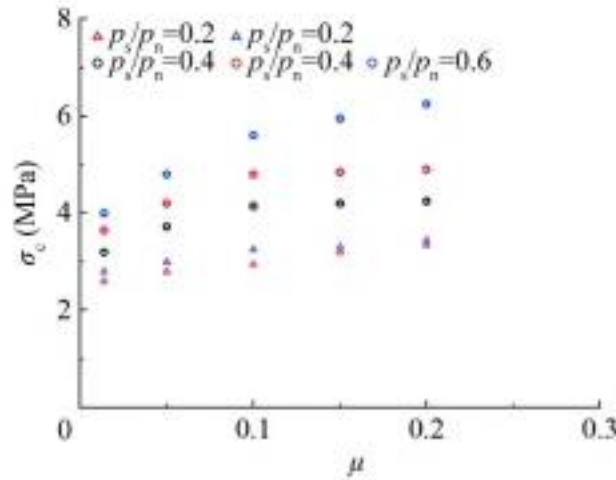

Fig. 17. Effect of L/D on mechanical properties of sea ice.

cles, and the local damage in uniaxial compression decreases the stability of the structure causing the compres-sive strength further reduced.

Modify Eqs. (25) and (26), we obtain:

$$b_{\mathrm{c}} = E_{\mathrm{c}}\left(\frac{LD}{L/D-1}\right)^2 \left(0.2423z^2 - 0.4689z + 0.6289\right);$$

$$b_{\mathrm{n}} = \sigma_{\mathrm{b}}\left(\frac{LD}{L/D-1}\right)^2 \left(0.741z^2 - 0.858z + 0.535\right).$$

After inspection, the cementation modulus and normal bonding strength of cementation are selected according to Eqs. (31) and (32), the simulation results can be consistent with the macro-mechanical parameters of sea ice and can accurately reflect the size effect of particles. 4.3 Correction considering the influence of friction coeffi-cient

The compressive strength is affected by the friction coefficient μ between the discrete element and the structure, and the degree of influence is related to the ratio of the tan-gential to normal stiffness of the cement. Fig. 18 shows the compression strength results under different friction coeffi-cients when the bending strength is the same. It can be seen from the figure that the compression strength increases with the increase of the friction coefficient.

Modify Eq. (24) to obtain:

$$= \begin{cases} \dfrac{-(2.5)M_P + B}{(0.5M_P + 0.5T_P + 0.0M_P)^2 + 0.0m_P - 10.4} \\ 0m_{e^{-0.5}} + 0.1m_P + 0.1 \end{cases}$$

After testing, the simulation results of the cemented tan-gential to normal stiffness ratio selected by the revised Eq. (33) conform to the set macroscopic mechanical parameters of sea ice and can reflect the influence of friction coeffi-cient more accurately. 5 Simulation of sea ice-structure interaction

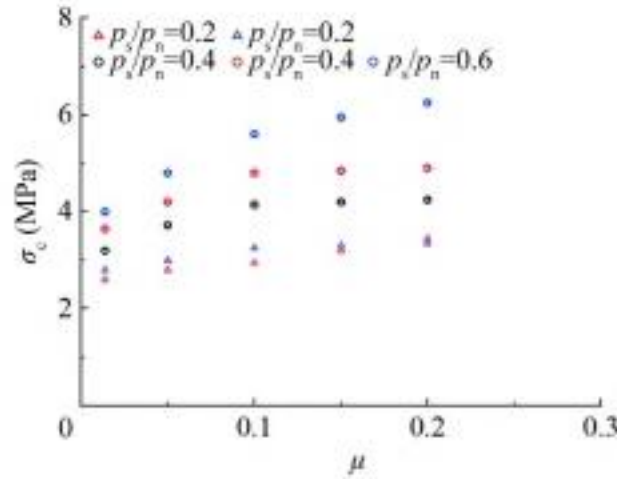In this section, the approach for selecting discrete element

Fig. 18. Effect of friction coefficient on compressive strength.

parameters of the common node DEM-SPH model is used to simulate the interaction process between sea ice and structures. The simulated sea ice failure mode, structural ice load characteristics and measured results are then compared and analyzed to validate the chosen discrete element param-eters in this paper. The accuracy of the formula is determined based on these findings.

8   5.1 Simulation of Bohai JZ20-2 MUQ plat-form and ice interaction

5.1.1 Numerical simulation setup

Dalian University of Technology has carried out ice load and structural vibration measurement work on the JZ20-2 MUQ platform in Bohai Sea for many years. The measured ice load results will be used as a reference below to evaluate the accuracy of the discrete element parameter selection for-mula of the common node DEM-SPH model.

The cone structure of the JZ20-2 MUQ platform in the Bohai Sea is composed of two parts: a forward cone and an inverted cone. The following research is the interaction between sea ice and the forward cone. As shown in Fig. 19, the inclination angle of the positive cone is $60°$,and the maximum and minimum diameters are 4 m and 1.7 m , respectively.

Fig. 20 shows the coupling model of sea ice-water-cone structure. The elastic modulus of the structural material is 2.1×10^5MPa ,Poissons ratio is 0.3,the compressive elastic modulus of sea ice is 1000MPa ,and the compressive intensity
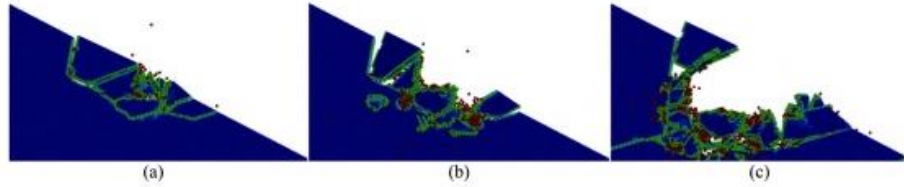

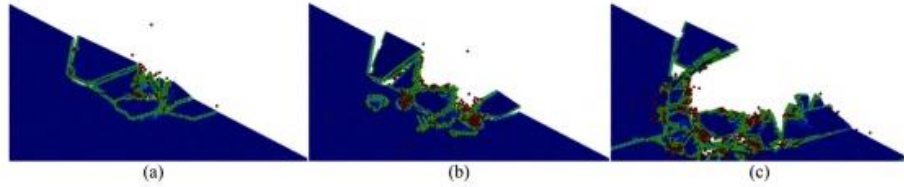Fig. 19. Dimension parameters of cone structure of JZ20-2 MUQ plat-form.

Fig. 20. Illustration of sea ice-water-cone structure interaction.

is 0.6MPa ,the ice thickness is 320 mm ,and the ice velocity is 430 mm/s . The relevant parameters used in the simulation are shown in Table 4.

9   5.1.2 Simulation results

Fig. 21 shows the comparison between the simulated results and the measured results in the Bohai Sea. It can be seen from the figure that during the interaction between sea

Table 4 Main parameter of interaction between sea ice and cone structure of JZ20-2 MUQ platform

Particle unit diameter D (mm)	121.6
Particle density ρ_{DEM} $\left(\text{t/mm}^3\right)$	8.0×10^{-10}
Particle elastic modulus E (MPa)	1000
Cementation modulus b_c (MPa)	1276
Ratio of bond tangential to normal stiffness p_s/p_n	0.363
Normal bond strength of cementation p_n (MPa)	0.5
Tangential bond strength of cementation p_s (MPa)	0.94
Coefficient of friction between sea ice and structure μ	0.1
Particle mass m_{SPH} (1)	9.42×10^{-5}
Density ρ_{SPH} $\left(\text{t/mm}^3\right)$	1.0×10^{-10}
Cut-off pressure P_C (MPa)	2.0×10^{-3}
Speed of sound c (mm/s)	1.65×10^{6}

ice and the cone structure, the sea ice mainly undergoes bending failure, and the sea ice breaks into fragments of a certain size. Fig. 22 shows the specific failure process of the interaction between sea ice and cone structures. The sea ice first cracks under the action of the cone structure, and then the sea ice breaks into several pieces of sea ice, as shown in Fig. 22a. The broken pieces of sea ice climb up along the slope of the cone structure, as shown in Fig. 22b. The broken ice then slides down along the surface of the structure, as shown in Fig. 22c. As a result, the sea ice completes a round of loading and unloading processes on the structure, and the load on the cone structure is continuously reciprocated under the action of sea ice, showing periodic changes.

Fig. 23 shows ice load time-history curve of the simulated interaction between sea ice and the cone structure of the JZ20-2 MUQ platform in the Bohai Sea. The maximum ice load is 158.0kN ,with an ice load period of 2.47 s ; the max-
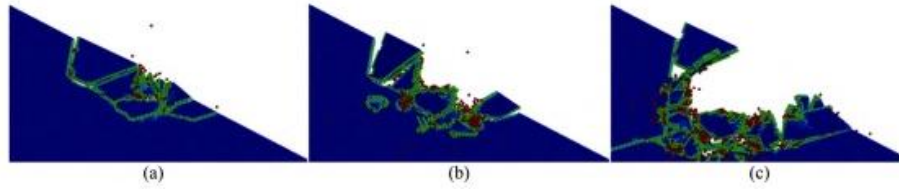

Fig. 21. Comparison between simulation results and measured results in the Bohai Sea.
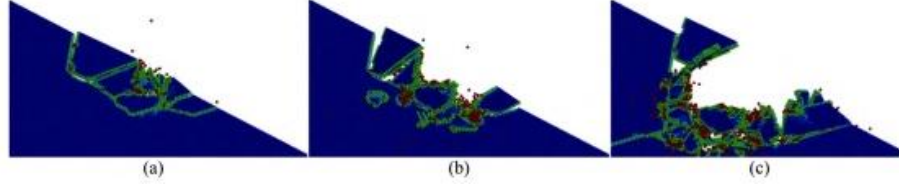
Fig. 22. Interaction between sea ice and the conical structure of JZ20-2 MUQ platform.
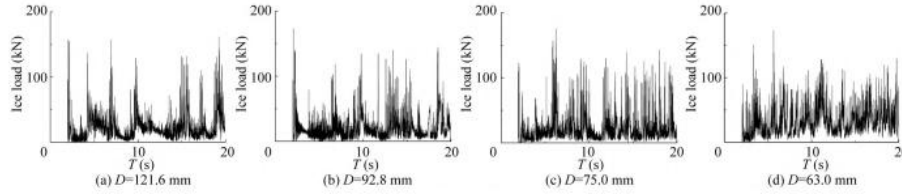
Fig. 23. Ice load of conical structure of JZ20-2 MUQ platform.

imum ice load measured in the Bohai Sea is 175.8kN ,with an ice load period of 2.43 s . Therefore,it can be seen from the action form, amplitude and period of the ice load that the equation for selecting the discrete element parameters of the common-node DEM-SPH model is accurate.

10   5.1.3 Influence of particle size

To further verify the accuracy of the equation for selecting discrete element parameters of the common node DEM-SPH model, four kinds of particle units with different diam-eters are selected to form flat ice, and the ice load results of the interaction between sea ice and cone structures under four-unit sizes are simulated and compared. During the sim-ulation process, the thickness of flat ice is kept the same, and the microscopic parameters of sea ice related to the par-ticle unit diameter are shown in Table 5.

Fig. 24 shows the time-history curves of ice loads simu-lated under four-unit sizes. Table 6 summarizes the calculated maximum ice loads and ice load periods. From the table, it can be seen that the maximum ice loads and ice load periods are consistent with those measured in the Bohai Sea. The data are relatively close, and the above results verify the accuracy of the discrete element parameter selection formula of the common-node DEM-SPH model.

23

11 5.2 Simulation of Bohai JZ9-3MDP pile legs and ice inter-action

Dalian University of Technology has carried out ice load measurements on Bohai JZ9-3MDP pile legs for several consecutive winters, and recorded parameters such as ice thickness and ice speed. The accuracy of the equation for selecting parameter is verified.

According to the actual size of the JZ9-3MDP pile legs in Bohai Sea, a sea ice-water-vertical structure coupling model is established with reference to Fig. 20. The elastic modulus of the structural material is $2.1{\times}10^5$MPa and Pois-son's ratio is 0.3 . According to the measured information of sea ice, the compressive elastic modulus of sea ice is 1000 MPa ,the compressive strength is 2.3MPa ,the bending strength is 0.8MPa ,the ice thickness is 180 mm ,and the ice velocity is 200 mm/s . The sea ice related parameters used in the simulation are shown in Table 7.

Fig. 25 shows the comparison between the simulated

Table 5 Microscopic parameters related to particle unit diameter

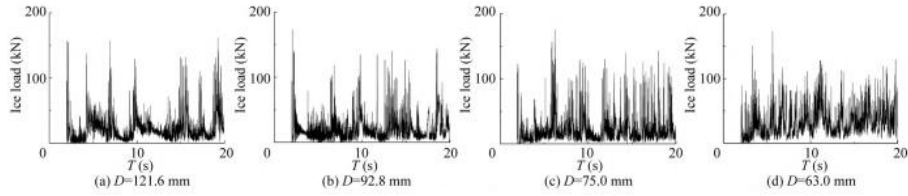|	
Particle unit diameter D (mm)	121.6
92.8	75.0
63.0	
Cementationmodulus b_e (MPa)	1276
973	837
761	
Normal bond strength of cementation b_{n} (MPa)	0.50
0.39	0.33
0.30	
Tangential bond strength of cementation b_{s} (MPa)	0.94
0.73	0.62
0.57	
Particle mass m_{SPH} (t)	$9.42{\times}10^{-5}$
$4.18{\times}10^{-5}$	$2.21{\times}10^{-5}$
$1.31{\times}10^{-5}$	

Fig. 24. Ice loading of ice sheet with different particle sizes

Table 6 Comparison of maximum ice load

Measured data from the Bohai Sea	–
175.8	2.43
Simulation 1	121.6
158.0	2.47
Simulation 2	92.8
173.0	2.35
Simulation 3	75.0
175.5	2.44
Simulation 4	63.0
173.3	2.17

Table 7 Main parameters of interaction between sea ice and JZ9-3MDP pile-leg structure

|	
Particle unit diameter D (mm)	68.4
Particle density ρ_{DEM} $\left(\mathrm{t/mm^3}\right)$	8.0×10^{-10}
Particle elastic modulus E (MPa)	1000
Cementation modulus b_{e} (MPa)	1294
Ratio of bond tangential to normal stiffness $p_s p_n$	0.34
Normal bond strength of cementation b_{n} (MPa)	0.684
Tangential bond strength of cementation b_{s} (MPa)	1.19
Coefficient of friction between sea ice and structure μ	0.1
Particle mass m_{SPH} (t)	1.70×10^{-5}
Density ρ_{SPH} $\left(\mathrm{t/mm^3}\right)$	1.0×10^{-10}
Cut-off pressure P_{C} (MPa)	5.0×10^{-2}
Speed of sound c (mm/s)	1.65×10^{6}
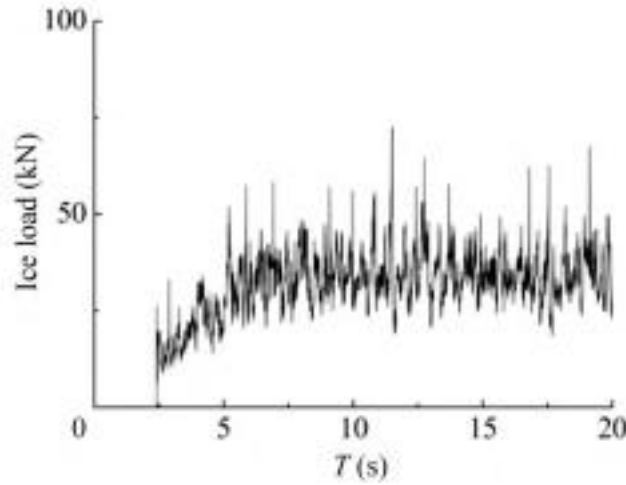
Fig. 25. Comparison between simulation results and measured results in the Bohai Sea.

25

results of the interaction between sea ice and JZ9-3MDP leg structures and the measured results in the Bohai Sea. The ice breaks up and presents as powdery flocs.

Fig. 26 shows the ice load of the JZ9-3MDP pile leg structure simulated by the DS-SPH method. The maximum ice load is 72.5kN ,which is smaller than the ISO standard calculation result of 988.2kN . This is due to the low ice force caused by non-simultaneous compression failure. The maximum ice load of the JZ9-3MDP pile leg measured in the Bohai Sea is about 60kN ,which is relatively close to the simulated ice load amplitude. Therefore, it can be con-sidered that the equation for selecting discrete element
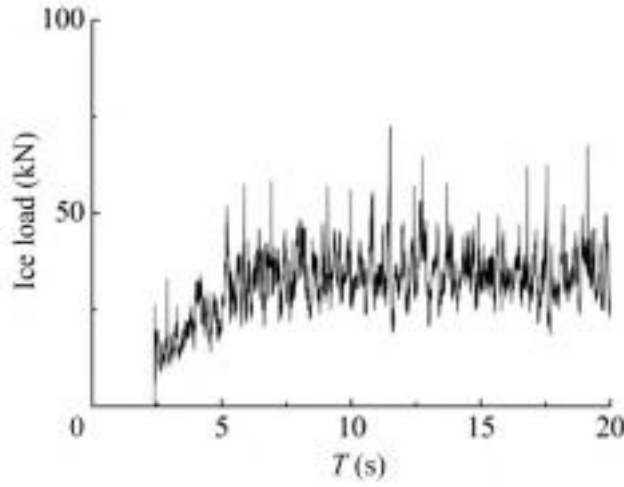

Fig. 26. Ice load of JZ9-3MDP pile leg structure simulated by DS-SPH method.

parameters of the common node DEM-SPH model is effec-tive.

12   6 Conclusions

This paper investigates the influence of DEM parameters and SPH particles on the macroscopic mechanical character-istics of sea ice under uniaxial compres-sion and three-point bending. Mathematical equations are also formulated to determine the elastic modulus of particles, as well as the normal and tangen-tial stiffness and bonding strength between particles, based on the compression elastic modu-lus, compression strength and bending strength of sea ice. The study includes a sensitivity analysis of particle radius and numerical verifica-tion, leading to the following conclu-sions.

(1) Incorporating SPH particles with fluid properties into the DEM model has little effect on the main mechanical parameters of sea ice, and it can avoid the particle splashing phenomenon when the cement fails. The compressive elas-tic modulus, flexural elastic modulus and cementation modulus exhibit a linear

26

positive correlation, as does the ratio between cemented tangential and normal stiffness. Com-pressive strength, bending strength and cemented bond strength also show a linear positive correlation. However, in cases where the bonding normal bonding strength remains constant, the bonding tangential bonding strength does not

impact the bending strength. By increasing the proportional factor for the contact stiffness, the actual compression deformation can be maintained constant, thereby reducing the elastic modulus of the particles and stabilizing the com-pression damage. Moreover, it is observed that the internal friction coefficient has no effect on the compressive strength and bending strength.

(2) The size of DEM particles and their friction coefficient with the structure critically influence the macroscopic mechanical properties of the common node DEM-SPH model. The DEM parameters chosen through the modified formula align with the designated macroscopic mechanical parameters of sea ice, effectively capturing the influences of particle size and friction coefficient.

(3) The common node DEM-SPH model is applied to simulate the interaction of sea ice, cone structure and vertical structure, respectively. The feasibility of the proposed method is validated by conducting a comparison between observed on-site data of structural ice load and sea ice fracture phenomena.

13   Competing interests

The authors declare no competing interests.

14   References

Di, S.C., Xue, Y.Z., Bai, X.L. and Wang, Q., 2018. Effects of model size and particle size on the response of sea-ice samples created with a hexagonal-close-packing pattern in discrete-element method simu-lations, Particuology, 36, 106-113.

He, K.J., Ni, B.Y., Xu, X.S., Wei, H.Y. and Xue, Y.Z., 2022. Numerical simulation on the breakup of an ice sheet induced by regular incident waves, Applied Ocean Research, 120, 103024.

Huang, L.F., Tuhkuri, J., Igrec, B., Li, M.H., Stagonas, D., Toffoli, A., Cardiff, P. and Thomas, G., 2020. Ship resistance when operating in floating ice floes: A combined CFD

DEM approach, Marine Struc-tures, 74, 102817.

Ji, S.Y., Di, S.C. and Long, X., 2017. DEM simulation of uniaxial compressive and flexural strength of sea ice: parametric study, Journal of Engineering Mechanics, 143(1), C4016010.

Ji, S.Y. and Tian, Y.K., 2021. Numerical ice tank for ice loads based on multi-media and multi-scale discrete element method, Chinese Journal of Theoretical and Applied Mechanics, 53(9), 2427-2453. (in Chinese)

Ji, S.Y., Wang, A.L., Su, J. and Yue, Q.J., 2011. Experimental studies on elastic modulus and flexural strength of sea ice in the Bohai Sea, Journal of Cold Regions Engineering, 25(4), 182-195.

Liu, L., Zhang, P., Xie, P.R. and Ji, S.Y., 2020. Coupling of dilated polyhedral DEM and SPH for the simulation of rock dumping process in waters, Powder Technology, 374, 139-151.

Liu, R.W., Xue, Y.Z., Han, D.F. and Ni, B.Y., 2021. Studies on model-scale ice using micro-potential-based peridynamics, Ocean Engi-neering, 221, 108504.Liu, R.W., Xue, Y.Z., Lu, X.K. and Cheng, W.X., 2018. Simulation of ship navigation in ice rubble based on peridynamics, Ocean Engi-neering, 148, 286-298.

Long, X., Ji, S.Y. and Wang, Y.F., 2019. Validation of microparameters in discrete element modeling of sea ice failure process, Particulate Science and Technology, 37(5), 550-559.

Luo, W.Z., Jiang, D.P., Wu, T.C., Guo, C.Y., Wang, C., Deng, R. and Dai, S.S., 2020. Numerical simulation of an ice-strengthened bulk carrier in brash ice channel, Ocean Engineering, 196, 106830.

Moslet, P.O., 2007. Field testing of uniaxial compression strength of columnar sea ice, Cold Regions Science and Technology, 48(1), 1-14.

Ni, B . and Huang,Q.,2020. Analysis of ice resistance in ice-structure interaction based on the cohesive element method, Proceedings of the 30th International Ocean and Polar Engineering Conference, ISOPE.

Ni, B.Y., Chen, Z.W., Zhong, K., Li, X.A. and Xue, Y.Z., 2020a. Numerical simulation of a polar ship moving in level ice based on a one-way coupling method, Journal of Marine Science and Engi-neering, 8(9), 692.

Ni, B.Y., Han, D.F., Di, S.C. and Xue, Y.Z., 2020b. On the development of ice-water-structure interaction, Journal of Hydrodynamics, 32(4), 629-652.

Sun, G.S., Di, S.C., Feng, Y.T. and Xue, Y.Z., 2023. Modelling the fracture behaviour of polycrystalline columnar ice using the grain-based discrete element method, Computational Particle Mechanics, doi: $10.1007/s40571-023-00595-w$

Tang, X.J., Zou, M., Zou, Z.J., Li, Z.Y. and Zou, L., 2022. A parametric study on the ice resistance of a ship sailing in pack ice based on CFD-DEM method, Ocean Engineering, 265, 112563.

Timco, G.W. and Weeks, W.F., 2010. A review of the engineering properties of sea ice, Cold Regions Science and Technology, 60(2), 107-129.

Wang, A.L., Xu, N. and Ji, S.Y., 2014. Characteristics of sea ice uniaxial compressive strength around the coast of Bohai Sea, The Ocean Engineering, 32(4), 82-88. (in Chinese)

Xie, C., Zhou, L., Wu, T.C., Liu, R.W., Zheng, S.J., Tsuprik, V.G. and Bekker, A., 2022. Resistance performance of a ship in model-scaled brash ice fields using CFD and DEM coupling model, Frontiers in Energy Research, 10, 895948.

Xue, Y.Z., Liu, R.W., Li, Z. and Han, D.F., 2020. A review for numerical simulation methods of ship-ice interaction, Ocean Engineering, 215, 107853.

Xue, Y.Z., Liu, R.W., Liu, Y., Zeng, L.D. and Han, D.F., 2019. Numerical simulations of the ice load of a ship navigating in level ice using peridynamics,

Computer Modeling in Engineering
Sci-ences, 121(2), 523-550.

Yang, B.D., Jiao, Y. and Lei, S.T., 2006. A study on the effects of microparameters on macroproperties for specimens created by bonded particles, Engineering Computations, 23(6), 607-631.

Yang, W.M., Wang, M.X., Zhou, Z.Q., Li, L.P., Yang, G. and Ding, R. S., 2020. Research on the relationship between macroscopic and mesoscopic mechanical parameters of limestone based on Hertz Mindlin with bonding model, Geomechanics and Geophysics for Geo-Energy and Geo-Resources, 6(4), 68.